Nano Research
2021, 14(11): 4063–4072

ISSN 1998-0124 CN 11-5974/O4
https://doi.org/10.1007/s12274-021-3341-z

Research Article

Metal-organic framework-derived Ni/ZnO nano-sponges with delicate surface vacancies as anode materials for high-performance supercapacitors

Anchun Tang, Chubin Wan (✉), Xiaoyu Hu, and Xin Ju (✉)

School of Mathematics and Physics, University of Science and Technology Beijing, Beijing 100083, China

Received: 29 September 2020 / **Revised:** 5 January 2021/ **Accepted:** 18 January 2021

ABSTRACT

Ni/ZnO nano-sponges have been successfully synthesized through optimized annealing of Ni/Zn-based organic framework (Ni/Zn-MOF). The annealed MOF provides the stable carbon structure with 3D interconnection and prevents structural collapse during the charging and discharging process. The annealing causes the incorporation of intrinsic Ni^{3+} in the surface of NiO nanoparticles, providing more reaction active sites. The oxygen vacancies in ZnO and heterostructure interfaces between NiO and ZnO promote the charge transformation. Based on the aforementioned advantages, the Ni/ZnO nanocomposites exhibit excellent electrocatalytic performances for supercapacitors. The specific capacitance can reach to 807 $F \cdot g^{-1}$ at 1 $A \cdot g^{-1}$ in the studied electrodes. After 5,000 cycles at 10 $A \cdot g^{-1}$, the cyclic stability remains excellent at 86% of the initial capacitance. Moreover, the as-prepared asymmetric supercapacitor exhibits a high energy density of 30.6 $W \cdot h \cdot kg^{-1}$ at power density of 398 $W \cdot kg^{-1}$. This study is expected to provide new insights into exploring the potential mechanism of catalyst action.

KEYWORDS

metal-organic frameworks, ZnO-based nano-sponges, surface vacancies, supercapacitor, electrochemical performance

1 Introduction

Efficient and eco-friendly energy harvesting and storage devices have garnered a tremendous amount of attention due to the depletion of fossil fuels and drastic deterioration of the environment [1–3]. As an energy storage device, a supercapacitor also known as ultracapacitor provides high power density, excellent cycling durability, and wide operating temperature range, it is considered to be a promising technology for the next-generation energy storage [4, 5]. In general, supercapacitor can be typically categorized into electric double-layer capacitor (EDLCs) and pseudocapacitor, which store energy by electrostatic accumulation and reversible Faraday redox reaction, respectively [6, 7]. Although great progress has been achieved in the past few decades, low energy density remains a concern in future applications [8, 9]. The overall properties of supercapacitors are governed by electrodes, separators, and electrolytes, but the electrode is a critical factor that determines the performance of supercapacitors [10]. Therefore, designing novel electrode materials through material engineering that can meet the requirements of supercapacitors and sustainable energy development is a challenge. In recent years, researchers have focused on studying transition metal oxides due to their strong electrochemical activities and rich redox reactions [11].

Among various transition metal oxides, zinc oxide (ZnO), a semiconductor material with piezoelectric properties, good photoelectric chemical activity, and mechanical stability, has been widely applied in sensors, electronics, and photocatalysts [12, 13]. Additionally, ZnO has become a prospective electrode material for supercapacitors because of its high specific energy density, good electrochemical activity, low cost, and non-toxicity [14]. However, pure ZnO shows slow Faraday redox kinetics and low electrical conductivity, which lead to poor capacitance and cycling stability of the electrode during rapid charging and discharging process [10]. Various strategies have been implemented to develop electrode materials with rapid charge transfer ability and long cyclic life. In general, coupling ZnO with carbon materials (such as activated carbon, graphene, and carbon nanotubes) and transition oxides with high specific capacitance was used as electrode materials. NiO is a promising battery-type material due to its high theoretical specific capacitance [15–17], and it is logical to improve the properties of electrode materials by doping NiO. In such carbon nanostructure-metal oxide composite electrodes, a synergistic effect could be expected and the materials cost can be reduced [18]. The deliberately incorporating defects into the lattice structure of host materials is considered as a new "intrinsic" strategy to increase electrical conductivity [19]. Recent investigations demonstrate that deficient transition metal oxides, such as ZnO, Co_3O_4, TiO_2, MnO_2, and V_2O_5, with high donor density can improve intrinsic conductivity and promote pseudocapacitive charge storage kinetics [20–22]. Sun et al. [23] reported single-crystalline ultrathin Co_3O_4 nanosheets with massive vacancy defects by mild solvothermal reduction. Electrochemical evidence indicated that this promoted performance was due to the larger electrochemical surface area, more favorable kinetics, and better electrical conductivity. Thus, inducing oxygen vacancies in ZnO and coupling with carbon

Address correspondence to Chubin Wan, cbwan@ustb.edu.cn; Xin Ju, jux@ustb.edu.cn

and NiO should be feasible for improving the electrochemical performance of ZnO-based hybrids.

Metal-organic framework (MOF) is a new porous material composed of metal ions and organic ligands [24, 25]. Structural tunability and flexible choice of elements make MOF a promising material widely used in many fields [26]. To date, various nanostructures have been successfully prepared using MOFs as precursors for energy storage and conversion devices [27]. High-temperature annealing of MOF materials is expected to induce surface defects in the nanostructure, thereby facilitating electron transfer. Jiao et al. [28] reported Ni/NiO microparticles with subtle lattice distortions by annealing Ni-MOF. The as-synthesized Ni/NiO nanoparticles exhibit specific capacitance of 684.4 $mF \cdot cm^{-2}$ at 1 $mA \cdot cm^{-2}$. Furthermore, carbon and metal oxide can be obtained simultaneously by annealing the MOF precursor in an inert atmosphere. However, to date, studies on the ZnO-based hybrids derived from MOF with abundant surface defects for supercapacitors are limited. The mechanism or certain effects of reaction or conductivity are not sufficiently clear.

In this study, we prepared Ni/Zn-based organic framework followed by a thermal decomposition process to produce the ZnO/Ni/NiO nanocomposite dispersed in carbon material with the interconnected 3D structure. We aim to explore the possible mechanism of catalyst reaction, and studied the crystal structure of ZnO and micro structures of Ni and NiO in the studied samples. The Ni/ZnO-600 (sample annealed at 600 °C) electrode shows the superior specific capacitance, rate capability, and long-term cycling stability. Present work might provide a new strategy to synthesize ZnO-based nanocomposites, which can be widely used to improve the electrochemical properties of supercapacitors.

2 Experimental

2.1 Synthesis of Ni-MOF precursor

All chemicals used are directly purchased without further purification. Typically, 0.3 g of nickel nitrate hexahydrate ($Ni(NO_3)_2 \cdot 6H_2O$) and 0.1 g of 1,4-benzenedicarboxylic acid (PTA) were dissolved in 30 mL of *N*, *N*-dimethylformamide (DMF) and 10 mL of ethylene glycol, the mixture was stirred at room temperature for 30 min. The solution was transferred to a 50 mL Teflon-lined autoclave and was sealed at 130 °C for 4 h. After reaction, the green product was washed several times with anhydrous ethanol and DMF, and dried at 70 °C overnight to obtain Ni-MOF.

2.2 Synthesis of Ni/ZnO-*X* (*X* = 400, 500, and 600)

Based on a previous report [26], 2D Zn-Hexamine coordination framework (Zn-HMT) was prepared by modified method. The previously as-prepared 60 mg of Ni-MOF and 0.5 g of hexamethylenetetramine were dissolved in 25 mL of absolute ethanol with vigorous stirring for 30 min; this is labeled as A solution. Then, 1 g of zinc nitrate hexahydrate ($Zn(NO_3)_2 \cdot 6H_2O$) was dissolved in 15 mL of absolute ethanol; this is labeled as B solution. Thereafter, the B solution was slowly poured into the A solution, and a pale green precipitate was formed immediately. After standing for 30 min, the precipitate was centrifuged and washed with ethanol several times. Thereafter, the sample was dried at 70 °C overnight. Finally, the as-synthesized Ni/Zn-MOF was annealed at 400, 500, and 600 °C for 2 h with the heating speed of 5 $°C \cdot min^{-1}$ under nitrogen current. The samples were labeled as Ni/ZnO-400, Ni/ZnO-500, and Ni/ZnO-600 to simplify the description.

2.3 Characterization

The phase structure of the samples was characterized by X-ray diffraction (XRD, Rigaku D/Max-2550 with Cu Kα radiation), and the scanning angle range is from 10° to 80° of 2θ with 0.02°/step. Raman spectroscopy was conducted on the samples using a JY-HR800 micro-Raman spectrometer with 532 nm excitation light. The morphological features were obtained through transmission electron microscopy (TEM, FEI Tecnai G2 F20) and field-emission scanning electron microscopy (FE-SEM, Zeiss Supra55 Sapphire) equipped with electron dispersive X-ray spectroscopy (EDS). The specific surface area (SSA) of the studied samples was measured using nitrogen cryosorption Micromeritics QuadraSorb Station 1. In addition, X-ray photoelectron spectroscopy (XPS) detection is performed on a Kratos Axis Supra.

2.4 Electrochemical measurement

Cyclic voltammetry (CV), galvanostatic charge and discharge (GCD), and electrochemical impedance spectroscopy (EIS) of all samples are conducted in a standard three-electrode configuration at room temperature using a CHI 660E electrochemical workstation. The mercury oxide electrode (Hg/HgO), platinum plate, and Ni/ZnO-*X* samples are invoked as the reference, counter, and working electrodes, respectively. The Ni/ZnO-*X* active material, acetylene black, and polytetrafluoroethylene (PTFE) are mixed in anhydrous ethanol at a mass ratio of 80:10:10 and ground carefully in an agate mortar. The resulting mixtures lightly coated on nickel foam have an effective area of 1 cm × 1 cm. Then, nickel foam was pressed into thin sheets, cleaned with anhydrous ethanol, and dried overnight in a vacuum oven at 80 °C.

The asymmetric supercapacitor (ASC) used Ni/ZnO-600 and commercial activated carbon as positive and negative electrodes, respectively. The two electrodes and separator form a sandwich structure to assemble the CR2032 coin-type cell with 3 M KOH electrolyte. The electrodes should be fully immersed in the electrolyte before testing.

3 Results and discussion

3.1 Sample preparation

Ni/ZnO-*X* (*X* = 400, 500, and 600) was synthesized following the process shown in Scheme 1. First, Ni-MOF nanospheres were prepared by hydrothermal method. Then, the Zn-HMT nanosheet was synthesized and coated with Ni-MOF to form a flower-like Ni/Zn-MOF. Finally, the precursors were annealed at different temperatures (400, 500, and 600 °C) under nitrogen atmosphere to obtain the target samples.

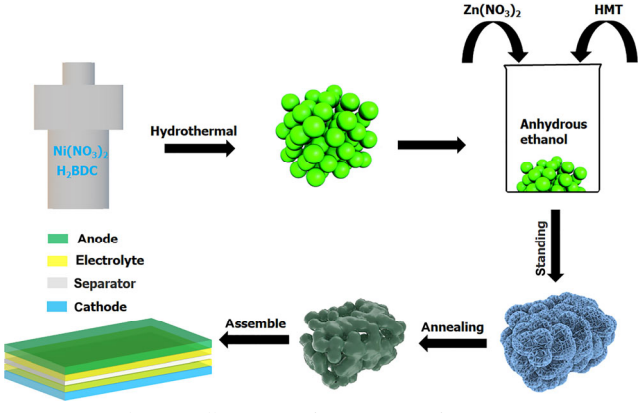

Scheme 1 Schematic illustration of preparation of Ni/ZnO-*X*.

3.2 XRD analysis

The XRD analysis was employed to confirm the crystallinity and crystal structures of the studied samples. As shown in Fig. 1, the sharp and highly intense diffraction peaks indicate high crystallinity of ZnO-based samples. The dominant diffraction peaks can be readily indexed to the hexagonal wurtzite structure of ZnO (JCPDS No. 36-1451, space group P63 mc). From the intensity and half width of ZnO peaks, the crystallization of ZnO nanoparticles increases with the increase of annealing temperature. The highly crystalline ZnO is expected to improve electrochemical performance [29]. The unit cell parameters of ZnO are reported in Table 1. The obtained ZnO cell dimensions are generally constant over the temperature range from 400 to 600 °C. All of the cell dimensions closely follow the lattice constants of hexagonal wurtzite structure (a = 3.2498 Å, c = 5.2066 Å) and a cell volume of 47.6 Å^3 [30]. The a/c value ratios remain the same in all the annealed samples, which means that ZnO maintains a stable structure after annealing. However, the cell volume of ZnO in Ni/ZnO-600 still increases by 0.5% compared with Ni/ZnO-400.

The average crystallite size of the ZnO nanoparticles is calculated on the basis of Debye–Scherrer formula (Table 1). The sample crystallite size increases with the increase of annealing temperature. The growth of nanoparticles is a thermal dependent process through the migration and diffusion of atoms. During high temperature annealing, crystal atoms gain energy to overcome the barriers between grains and move freely through the lattice by diffusion [31, 32]. At 600 °C, the process of coalescence might cause major grain growth, which small crystallites coalesce together to make larger crystallites [33]. The increase of crystal size can be attributed to the decrease of surface potential energy [34]. And the sudden increase of Ni/ZnO-600 crystal size was observed. Compared with those reported in other studies [29], the nanoparticles of ZnO in our work are relatively small. This condition is due to the presence of carbon structure originating from MOF materials, which prevents particles from agglomerating.

In addition, although no clear diffraction peaks are shown in Fig. 1, the amorphous carbon still exists in the studied samples, which can be confirmed by the following XPS and Raman analysis. The carbon materials can improve conductivity and provide a stable structure for the nanocomposites. The ZnO-carbon electrode with enhanced capacitive behavior and improved cycling life has been confirmed in previous studies [35, 36].

Moreover, a distinct bulge of approximately 43° is observed in Ni/ZnO-400, which corresponds to the (200) plane of NiO (JCPDS No. 47-1049). The spectral line broadening of NiO may be due to the low crystallinity. However, no obvious signals can be seen in Ni/ZnO-500 and Ni/ZnO-600. According to the subsequent Raman spectrum and X-ray photoelectron spectrum results, we believe that NiO still exists in Ni/ZnO-500 and Ni/ ZnO-600, but it cannot be reflected in the XRD pattern because of its low content and low crystallinity. Ni nanoparticles exist in all studied samples, as revealed by its XRD profile where the peaks at 44.3°, 51.7°, and 76° can be assigned to the (111), (200), and (220) planes of the Ni substrate (JCPDS No.89-7128), respectively. Furthermore, Fig. 1 shows that more NiO is converted into Ni at high temperature. This condition can be attributed to the reduction reaction of NiO to form Ni in higher annealing temperature. Different valence states of nickel in the samples may further influence the structure and electrochemical properties, as discussed in the following sections.

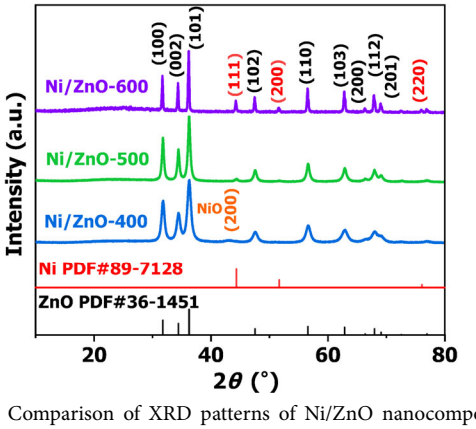

Figure 1 Comparison of XRD patterns of Ni/ZnO nanocomposites to PDF of bare ZnO and Ni.

Table 1 Unit cell parameters of ZnO as a function of annealing temperature of synthesized samples

Sample	a/b (Å)	c (Å)	a/c	Cell volume (Å^3)	Crystal size (nm)
Ni/ZnO-400	3.2487	5.2090	0.62	47.61	12.4
Ni/ZnO-500	3.2501	5.2084	0.62	47.64	19.8
Ni/ZnO-600	3.2571	5.2110	0.62	47.87	48.1

3.3 Raman analysis

Raman spectroscopy is an effective method for studying the metal-oxygen bond vibrations and structural defects of nanocomposite [37]. As shown in Fig. 2, Raman scattering spectra of the Ni/ZnO-X ranging from wavenumber 200 to 2,000 cm^{-1} were observed at room temperature. The Raman peaks of the samples after high-temperature annealing may shift and overlap. To facilitate the analysis, we used Gaussian function to separate and fit the Raman peaks.

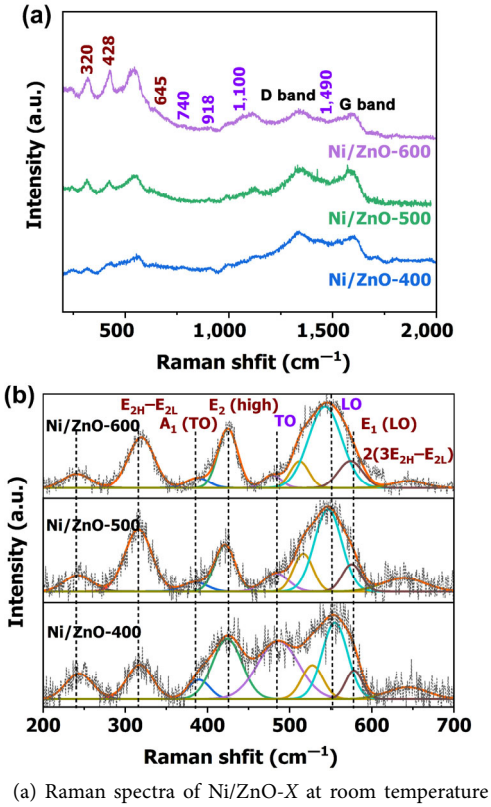

Figure 2 (a) Raman spectra of Ni/ZnO-X at room temperature (λ_{exc} = 325 nm) and (b) Gaussian curve fitting of Raman spectra of Ni/ZnO-X in the range of 200–700 cm^{-1}.

According to group theory, the ZnO with a hexagonal Wurtzite structure is classified as P63 mc, which predicts the optical phonons $A_1 + 2B_1 + E_1 + 2E_2$ [38]. B_1(low) and B_1(high) modes are Raman inactive. Both A_1 and E_1 are split into longitudinal (LO) and transverse (TO), which are related to the propagation perpendicular to the C axis of symmetry [37]. The Raman-active modes appear in all of the studied samples, similar to those commonly reported for ZnO [37–39].

As shown in Fig. 2, the bands observed at 320, 380, and 428 cm^{-1} are attributed to the E_{2H}–E_{2L}, A_1(TO), and E_2 (high) Raman active phonon modes of ZnO [38]. In general, the E_2 (high) vibration mode is dominant in the Raman spectrum of hexagon wurtzite structure, but its intensity is sharply weakened after doping. The Raman peak located at 643 cm^{-1} indicates the vibration of 2 ($3E_{2H}$–E_{2L}). The broad bands in the range of 950–1,200 cm^{-1} (except 1,100 cm^{-1}) correspond to a combination of TO and LO modes of ZnO [40].

The photon mode at 578 cm^{-1}, which is labeled as E_1 (LO) vibrational mode, is related to oxygen vacancies. The stronger intensity and broadening of the mode suggest that the oxygen vacancy concentration has increased in the studied samples with the increased in annealing temperature, and similar results were observed in previous research [41]. The oxygen vacancies can promote charge transport and ion diffusion [42, 43].

According to the results presented in Fig. 2, the vibration mode of NiO is also selected in addition to that of ZnO. The two peaks at 486 and 554 cm^{-1} can be assigned to the first-order transverse and longitudinal optical phonon modes [44]. Meanwhile, the bands centered at 740, 918, and 1,100 cm^{-1} are attributed to the 2TO, TO+LO, and 2LO vibrational bands. The peak at 1,490 cm^{-1} is classified as two-magnon excitation (2M). Compared with Ni/ZnO-400, the two other samples show a significantly decreased intensity of the TO mode. This result may be related to the NiO reduction.

Although the LO scattering is Raman inactive in the perfect NiO crystal structure, weak lattice distortion or the presence of defects make it visible [45]. The intensity of the LO Raman mode is closely related to the stoichiometric ratio of the elements and increases with the Ni vacancy concentration in the crystal lattice [46]. As shown in Fig. 2(b), an increase in the first LO vibration mode is observed with the increase of annealing temperature. The high intensity of LO mode in Ni/ZnO-600 indicates the presence of abundant nickel vacancies. The nickel vacancies introduced in NiO can provide more electrochemical active sites and improve supercapacitive performance of the nanocomposite [28].

However, anomalous Raman modes at 247 and 537 cm^{-1} are identified from all of the annealed samples, which do not correspond to the first-order or second-order active modes of ZnO and NiO. To date, their origin remains unclear, as previous studies provide inconsistent interpretations. Kaschner et al. [47] showed that the anomalous peaks were associated with N-related local vibrational modes. Some studies have also reported this phenomenon in N-doped ZnO samples [48, 49]. However, Manjón et al. [50] pointed out that the anomalous peaks were due to silent ZnO Raman modes (B_1 (low) and $2B_1$ (low)) allowed by the breakdown of the translational crystal symmetry induced by defects and impurities. In addition, the Raman peak at 537 cm^{-1} can be derived from surface optical (SO) phonon mode of NiO. In general, a first-order magnon background exists over the first-order phonon mode, so the SO mode is indistinguishable and rarely reported [46]. The appearance of SO mode suggests that the nanoparticles are imperfect [45].

In addition, the two characteristic peaks of D-band (approximately 1,350 cm^{-1}) and G-band (approximately 1,590 cm^{-1}) are clearly visible, confirming the presence of carbon. The G band is associated with graphite carbon with sp^2 hybridized carbon [51]. The intensity ratio (I_D/I_G) is typically used to measure the graphitic order of carbon materials [52]. The I_D/I_G value of Ni/ZnO-400, Ni/ZnO-500, and Ni/ZnO-600 are calculated to be approximately 1.79, 1.55, and 1.48, respectively (as shown in Fig. S1 in the Electronic Supplementary Material (ESM)). Obviously, the graphitization degree of carbon materials is related to the annealing temperature. The lower I_D/I_G value of Ni/ZnO-600 demonstrates a high graphitization degree, which inevitably results in good electrical conductivity [51]. No vibration mode of nickel nanoparticles can be observed in the shape of the Raman spectra.

3.4 SEM and TEM analysis

Morphological analysis of the obtained samples was performed using SEM and TEM. Figure 3 shows a typical SEM image of the as-prepared samples. The Ni-MOF presents a smooth spherical structure with a diameter of approximately 300 nm (Fig. S2 in the ESM). The Zn/Ni-MOF precursor has a unique interconnected 3D structure and a flower-like shape that is evident at high magnification (as shown in the bottom-right inset in Fig. 3(a)). Apparently, nanosphere Ni-MOF plays an

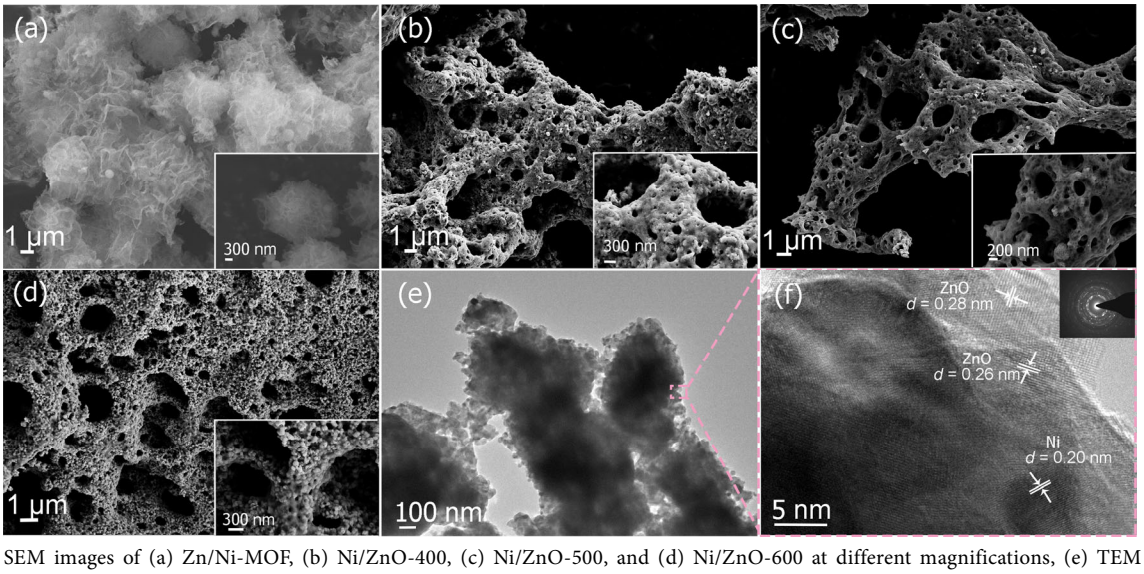

Figure 3 SEM images of (a) Zn/Ni-MOF, (b) Ni/ZnO-400, (c) Ni/ZnO-500, and (d) Ni/ZnO-600 at different magnifications, (e) TEM image of Ni/ZnO-600, and (f) corresponding HRTEM and SAED image of Ni/ZnO-600.

important role in the construction of 3D networks. Interestingly, the morphology of the precursor changes greatly after annealing. All of the studied samples show a stable 3D framework structure with nanoscale and microscale porosity. Figure 3(b) displays the SEM images of the Ni/ZnO-400, and ZnO nanoparticles are connected with staggered nanospheres. Based on XRD analysis, NiO is reduced to metal Ni after annealing, which results in the destruction of the nanospheres. This condition can be confirmed in the pictures of Ni/ZnO-500 and Ni/ZnO-600, as shown in Figs. 3(c) and 3(d)), both of which indicate a bread-like sponge structure.

A closer look shows that as the annealing temperature increases, the size of ZnO nanoparticles also grows. According to thermodynamics, higher annealing temperature provides more thermal energy to the system. The diffusion and collision rates of the particles are increased, thereby facilitating the particle aggregation.

High-temperature annealing provides defect-free interfacial contacts between carbon and ZnO. Nanostructured surfaces of carbon and ZnO can increase the effective surface area for more reaction sites [29]. As shown in Fig. S3 in the ESM, EDS analysis was carried out to determine the elemental composition of the studied samples. The elemental mapping spectra of Ni/ZnO-600 show in Figs. S3(d)–S3(g) in the ESM, diagrams of Zn, O Ni, and C show uniform distribution of elements on the sample surface. By comparing EDS of annealed samples (Figs. S3(a)–S3(c) in the ESM) at different temperatures, a nonstoichiometric oxygen deficiency is observed, indicating the formation of oxygen vacancies within the nanocrystals under high temperature anoxic annealing [29]. Although EDS is a qualitative analysis tool and might not be sufficient for element quantification. Raman and XPS analyses (Figs. 2 and 4(c)) also confirm the variation of oxygen deficiency in the samples.

In addition, TEM images of Ni/ZnO-600 are shown in Fig. 3(e). The sample consists of tightly connected and well-crystallized ZnO grains. The TEM results of the other two samples are presented in Figs. S4(a) and S4(b) in the ESM. In Figs. S4(e)–S4(g) in the ESM, by evaluating the sizes of particles from a closer inspection of the TEM micrographs, the size distributions were obtained. An increase in grain size with increasing annealing temperature is also observed. The average particle size of Ni/ ZnO-400, Ni/ ZnO-500, and Ni/ ZnO-600 are 13.3, 21.1, and 45.2 nm, respectively. High-resolution transmission electron microscopy (HRTEM) imaging confirmed that these samples are highly crystalline. As shown in Fig. 3(f), Ni/ZnO-600 presents characteristic spacings of 0.28 and 0.26 nm for the (100) and (002) lattice planes of hexagonal ZnO. The expected spacing of 0.20 nm is on the (111) plane of Ni. The selected area electronic diffraction (SAED) analysis shows that the sample has a polycrystalline structure. According to the HRTEM of Ni/ZnO-400 and Ni/ZnO-500 (Figs. S4(c) and S4(d) in the ESM), the lattice fringe of ZnO and NiO can be observed in Ni/ZnO-400, ZnO, and Ni present in Ni/ZnO-500. The preceding analyses are consistent with the XRD results.

The nitrogen adsorption and desorption isotherm curves of samples annealed at different temperatures of 400, 500, and 600 °C are shown in Fig. S5 in the ESM. According to the IUPAC nomenclature, all of them can be classified as type IV isotherms with type H3 hysteresis loop at the relative high pressures, which is a characteristic of mesopores [32]. The SSA of Ni/ZnO-400, Ni/ZnO-500, and Ni/ZnO-600 are 53.8, 42.5, and 40.3 m^2/g, respectively. The surface area decreased at higher annealing temperatures may be related to particle size growth. High temperature annealing makes nanoparticles agglomerate and the specific surface area decreases correspondingly [53, 54].

3.5 XPS analysis

The elemental composition and surface chemical state of the samples were characterized by XPS. Figure 4(a) shows the wide scans of the studied samples, which indicate the existence of Zn, O, Ni, and C. As shown in Figs. 4(d)–4(f), the dominant peaks of the binding energies at 856 and 873.6 eV correspond to the Ni $2p_{3/2}$ and Ni $2p_{1/2}$ signals of Ni^{3+}, while the binding energies at 853.5 and 871.1 eV are attributed to the Ni $2p_{3/2}$ and Ni $2p_{1/2}$ signals of Ni^{2+}. XPS studies confirm the coexistence of Ni^{3+} and Ni^{2+}. The predominance of Ni^{3+} suggests that vacancies of Ni are successfully introduced into the lattice of Ni/NiO during annealing. Ni^{2+} is oxidized to Ni^{3+} to maintain electrostatic balance near surface Ni vacancies. These results are in good agreement with the Raman spectrum. The area ratio

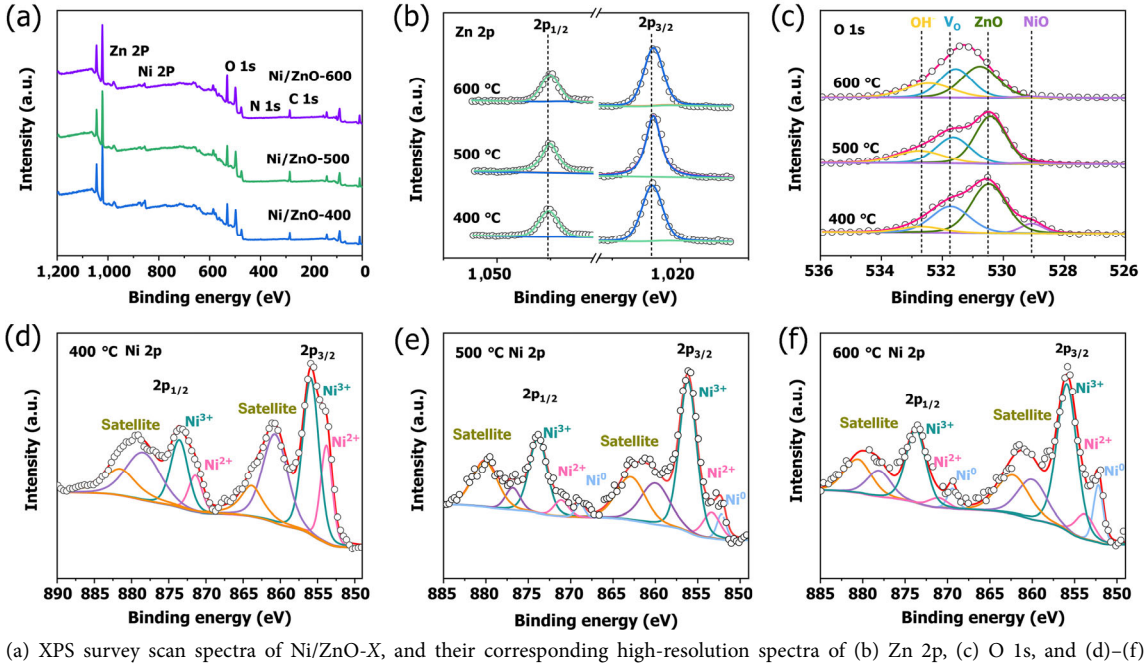

Figure 4 (a) XPS survey scan spectra of Ni/ZnO-*X*, and their corresponding high-resolution spectra of (b) Zn 2p, (c) O 1s, and (d)–(f) Ni 2p of Ni/ZnO-*X* (400, 500, and 600).

of the fitting peak corresponds to its content ratio. The area proportion of fitted peaks of Ni^{3+} in Ni/ZnO-400, Ni/ZnO-500, and Ni/ZnO-600 are 68.9%, 76.2%, and 79.2%, respectively (Table S1 in the ESM). It can be seen that nickel vacancy concentration in Ni/ZnO-600 is higher than that of other samples. The electrochemical performance of 3d transition metal-based electrocatalysts highly depends on the occupancy of e_g orbitals. Transition metal oxides with extremely low or extremely high e_g occupancy (0 or 2) result in unsatisfactory water-splitting properties [55]. In general, bulk NiO is caused by $t_{2g}^6e_g^2$ electronic configuration. The abundance of nickel vacancies in Ni/ZnO is expected to produce Ni^{3+} sites ($t_{2g}^6e_g^1$) and generate a local lopsided Coulomb force [28, 55]. The subtle distortion in the NiO lattice can provide additional active sites for the electrochemical reaction.

Furthermore, the two fitting peaks at 852.2 and 869.4 eV belong to Ni^0 and an increase of Ni^0 component is observed at higher annealing temperatures. The presence of metal Ni can effectively improve the electrical conductivity and corrosion resistance of the electrode materials.

The core-level spectra of the O 1s peak are used to investigate the oxygen vacancies in the samples. As illustrated in Fig. 4(c), the asymmetric O 1s peak is deconvoluted into four Gaussian peaks, namely, 529 eV in Ni–O, 530.5 eV in Zn–O, 531.7 eV in O–deficient regions, and 532.7 eV corresponding to O in OH^-, H_2O, and the chemisorption peaks. The results show that a large number of surface O vacancies are produced during annealing in N_2 atmosphere. The area proportion of fitted peaks of oxygen vacancy (V_o) for Ni/ZnO-400, Ni/ZnO-500, and Ni/ZnO-600 are 30.1%, 31.4%, and 32.9%, respectively (Table S2 in the ESM). An increase in O deficiencies in the samples is also observed with an increase in the annealing temperature.

Oxygen vacancy also can play a crucial role in improving the photo/electrochemical performance of metal oxides. Recent studies [22, 23, 29, 55] have reported that O vacancy in ZnO, TiO_2, V_2O_5, and Co_3O_4 increases donor density, thereby intrinsically enhancing the conductivity.

We also capture some variations in the energy spectrum of Zn 2p (Fig. 4(b)). A pair of strong peaks in Ni/ZnO-400 with binding energies of 1,022 and 1,045.1 eV are visible, which are classified as Zn $2p_{3/2}$ and Zn $2p_{1/2}$, respectively. The spin-orbit splitting of 23.1 eV demonstrates the presence of divalent zinc. However, in the core-level Zn 2p spectrum of Ni/ZnO-600, these characteristic peaks are located at 1,021.6 and 1,044.7 eV. Obviously, a negative shift in the binding energy of Zn^{2+} can be found, indicating that the electron density of Zn^{2+} increased [56]. This result can be attributed to the formation of oxygen vacancies during annealing. Similarly, to keep the charge balance around the formed oxygen vacancies, the electron density of surface Zn^{2+} is increased. ZnO may draw electrons from NiO, this unique electronic structure of Ni/ZnO with the predominance of Ni^{3+} and V_o results in high electrical conductivity and facilitates efficient charge transfer [55]. Moreover, C 1s spectrum (Fig. S6 in the ESM) is divided into four peaks at 284.8, 286.1, 288.5, and 289.2 eV, which can be allotted to C=C/C–C, C–N, C=O, and π–π*.

3.6 Electrochemical characterization of Ni/ZnO-*X*

The electrochemical properties of the as-prepared Ni/ZnO-400, Ni/ZnO-500, and Ni/ZnO-600 are evaluated using a three-electrode system in 3 M KOH electrolyte. As shown in Fig. 5(a), the CV results at scan rate of 50 $mV·s^{-1}$ are within the potential range of 0–0.7 V. All the CV curves are similar in shape, and a pair of obvious redox peaks indicate the main pseudocapacitance behavior.

The possible Faraday processes in our experiment are as follows:

$$ZnO + OH^- \leftrightarrow ZnOOH + e^- \quad (1)$$

$$NiO + OH^- \leftrightarrow NiOOH + e^- \quad (2)$$

The transformations of $Zn^{2+} \leftrightarrow Zn^{3+}$ and $Ni^{2+} \leftrightarrow Ni^{3+}$ proceed during the charge and discharge processes. Obviously, the CV curve of Ni/ZnO-600 sweeps the largest area within the same voltage window, revealing higher-charge storage levels and better electrochemical behavior. As presented in Fig. 5(b), the voltage platform of each GCD curve corresponds to the redox peak in the CV curve. Based on the GCD, the specific capacitances of Ni/ZnO-400, Ni/ZnO-500, and Ni/ZnO-600 at a current density of 1 $A·g^{-1}$ are calculated to be 315, 515, and 807 $F·g^{-1}$, respectively.

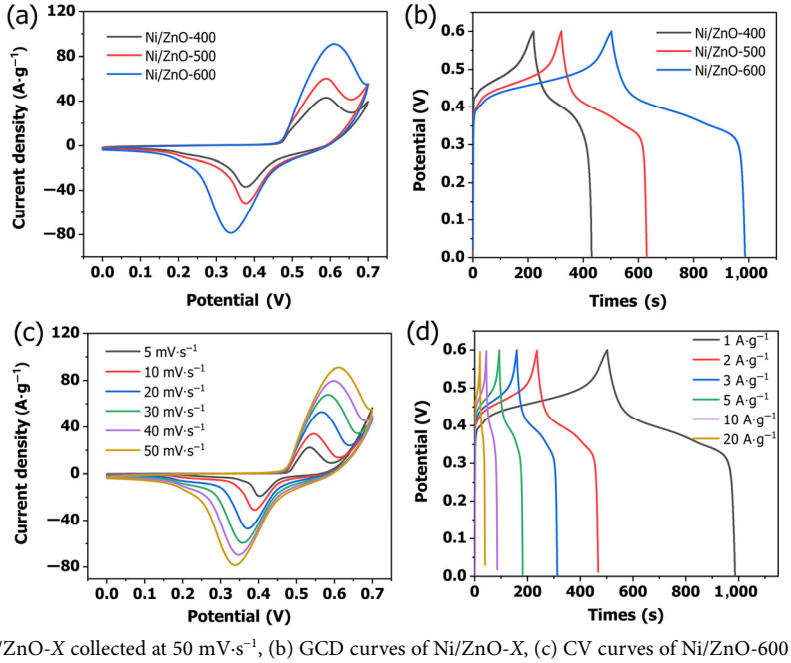

Figure 5 (a) CV curves of Ni/ZnO-*X* collected at 50 $mV·s^{-1}$, (b) GCD curves of Ni/ZnO-*X*, (c) CV curves of Ni/ZnO-600 at different scan rates, and (d) GCD curves of Ni/ZnO-600 at various current densities.

As the Ni/ZnO-600 electrode has the best supercapacitor performance, it has to be discussed in detail. The CV responses of Ni/ZnO-600 at different scanning rates between 5 and 50 mV·s^{-1} are presented in Fig. 5(c). All of the CV curves maintain a similar shape. Even at the high scanning rate of 50 mV·s^{-1}, the shape of the CV curve does not change significantly, which demonstrates that the Ni/ZnO-600 electrode has good kinetic reversibility. Due to the increase of the internal diffusion resistance and polarization of the electrode material, the peak current increases with rising scan rates. The CV curves of Ni/ZnO-400 and Ni/ZnO-500 are also presented in Figs. S7(a) and 7(b) in the ESM. In addition, the constant current discharge curves of Ni/ZnO-600 under various current densities are reported in Fig. 5(d). The calculated gravimetric capacitances are 807, 770, 755, 708, 627, and 508 F·g^{-1} at different current densities in the range of 1–20 A·g^{-1}. The GCD of the other two samples are also shown in Figs. S7(c) and S7(d) in the ESM.

The decrease of capacitance of the electrode at higher current density may contribute to high ionic diffusion resistance, slow electrolyte penetration, and insufficient reversible redox reaction of active materials [57, 58]. To show the advantages of the Ni/ZnO-600, we compare the performance of ZnO-based electrodes in the supercapacitor in Table 2. For instance, Ni/ZnO-600 exhibits excellent specific capacitance in lower-concentration KOH electrolyte compared with ZnO nano-membranes (NMs) [35]; this condition also shows a slightly wider operating voltage than ZnO/NiO [60] when tested in 3 M KOH.

Furthermore, the relationship between the specific capacitance and current density of Ni/ZnO-*X* electrodes is shown in Fig. 6(a). At a high current density of 20 A·g^{-1}, Ni/ZnO-400, Ni/ZnO-500, and Ni/ZnO-600 maintain a specific capacitance of 38%, 56%, and 63%, respectively. The Ni/ZnO-600 reveals an outstanding rate capability, which is an important property of supercapacitors. Figure 6(b) demonstrates the cycle performance of the electrodes. After 5,000 cycles at a current density of 10 A·g^{-1} in 3 M KOH solution, Ni/ZnO-600 maintains 86% of its initial capacitance, which is superior to that of the Ni/ZnO-400 (78%) and Ni/ZnO-500 (82%) electrodes.

The EIS was used to further analyze the conductivity and capacitive behavior of the electrode material. The corresponding Nyquist diagram is displayed in Fig. 6(c). In the low-frequency region, the slope of the curve is related to the diffusion process. In the high-frequency region, it contributes to the Faradic reactions and its diameter represents the Faradaic charge-transfer resistance at the electrolyte–electrode interface. When the high-frequency region of the Ni/ZnO-600 is magnified, no semicircle is observed, which indicates that the charge transfer resistance is relatively small. The low-charge transfer resistance is related to the sufficient and efficient electrochemical reaction sites. Moreover, compared with the other two electrodes, the slope of Ni/ZnO-600 in the low-frequency region is larger, indicating its low diffusion resistance.

The low diffusion resistance can promote the ion diffusion in the redox reaction process. The preceding results confirm that the effective electron transfer and fast ion diffusion are responsible for the outstanding electrochemical performance of the Ni/ZnO-600.

To further demonstrate whether the promoted specific capacitance of Ni/ZnO-600 is contributed by pure NiO or its own special structure, we annealed Ni-MOF and Zn-HMT at 600 °C in an N_2 atmosphere for 2 h to obtain NiO and ZnO, respectively. The CV and GCD tests of pure NiO and ZnO are conducted in a standard three-electrode configuration at room temperature. The CV responses of ZnO and NiO at different scanning rates between 5 and 50 mV·s^{-1} are presented in Figs. S8(a) and S8(b) in the ESM. A pair of distinct redox peaks can be seen in the CV curves of ZnO and NiO. By comparing the redox peak position of ZnO, NiO, and Ni/ZnO-*X*, it can be found that the peak position of ZnO is very close to that of Ni/ZnO-*X*. And the redox peak position of pure NiO shifted to low voltage obviously. Figures S8(c) and S8(d) in the ESM show the GCD curves of pure ZnO and NiO under various current densities. The calculated capacitances of pure ZnO are 290, 266, 253, 237, 213, and 188 F·g^{-1} at different current densities in the range of 1–20 A·g^{-1}. And the calculated capacitances of pure NiO are 438, 414, 398, 377, 342, and 300 F·g^{-1}. The

Table 2 Comparison of electrochemical performance of Ni/ZnO-600 with reported ZnO-based electrodes in supercapacitor

Sample	Current density (A·g^{-1})	Specific capacitance (F·g^{-1})	Electrolyte	Voltage window (V)	Ref.
Ni/ZnO-600	1.0	807	3 M KOH	0–0.6	This work
ZnO-Au	2.0	205.7	2 M KOH	0–0.58	[59]
ZnO NMs	1.0	846	6 M KOH	0–0.6	[35]
ZnO/NiO	1.0	435.1	3 M KOH	0–0.5	[60]
ZnO/nitrogen-doped hierarchically porous carbon (NOHPC)	1.0	720	6 M KOH	0–0.5	[61]
ZnO/CeO_2	3.0	495.4	3 M KOH	0–0.4	[57]
ZnO/MnO_x	1.0	556	1 M Na_2SO_4	0–0.9	[62]
Al_2O_3-ZnO	1.0	463.7	1 M Na_2SO_4	0–0.6	[63]

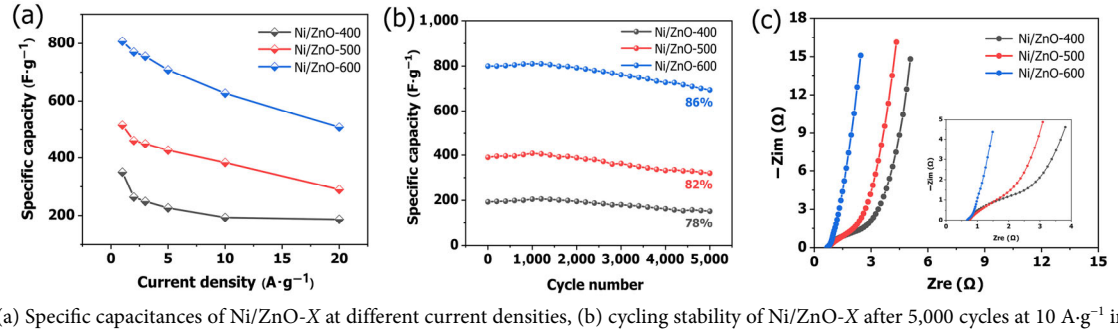

Figure 6 (a) Specific capacitances of Ni/ZnO-*X* at different current densities, (b) cycling stability of Ni/ZnO-*X* after 5,000 cycles at 10 A·g^{-1} in 3 M KOH solution, and (c) Nyquist plots of Ni/ZnO-*X*.

specific capacitance of NiO is expected to be slightly higher than that of ZnO. However, compared with Ni/ZnO-600 (807 $F \cdot g^{-1}$), the specific capacitance of pure NiO and ZnO are much smaller.

Based on the preceding results, the better electrochemical performance of the Ni/ZnO-600 can be attributed to the following factors: (1) The unique 3D framework structure shortens the way of ion transport. (2) Carbon and metal oxides derived from MOF materials produce a synergistic effect. (3) The presence of nickel nanoparticles can effectively improve the conductivity and corrosion resistance of the electrode material, thereby improving the specific capacitance and cycling performance. (4) Abundant Ni^{3+} sites exist in the form of NiOOH, providing more electrochemical active sites for redox reactions. (5) Oxygen vacancies in ZnO significantly improve the charge-transfer efficiency by improving the donor density.

3.7 Electrochemical performance of ASC (Ni/ZnO-600)

To further evaluate the prospect of Ni/ZnO-600 in practical application, an asymmetric supercapacitor device is assembled by employing Ni/ZnO-600 as the positive electrode, activated carbon as the negative electrode, and 3 M KOH as the electrolyte. Meanwhile, the storage charge between the two electrodes should be balanced, the load mass of the positive and negative electrodes is determined by Eq. (3):

$$\frac{m_+}{m_-} = \frac{C_- \times \Delta V_-}{C_+ \times \Delta V_+} \tag{3}$$

where m is the mass of the positive and negative electrodes. C and V denote the specific capacitance and potential windows of the two electrodes.

As shown in Fig. 7(a), the CV curves of the device are tested between 0 and 1.6 V at different scanning rates in the range of 5–50 $mV \cdot s^{-1}$. The final shape is contributed by the Faraday pseudo-capacitor and EDLC capacitor simultaneously. Based on the GCD curves (Fig. 7(b)), the specific capacity calculated at different current densities (1–10 $A \cdot g^{-1}$) are 97.6, 79.3, 67.8, 58.5, 54.6, and 23.2 $F \cdot g^{-1}$, respectively. Moreover, the energy density (E) and power density (P), as important characteristics of energy storage equipment, can be calculated based on Eqs. (4) and (5):

$$E = \frac{0.5C(\Delta V)^2}{3.6} \tag{4}$$

$$P = \frac{3{,}600E}{\Delta t} \tag{5}$$

where C ($F \cdot g^{-1}$), Δt (s), and ΔV (V) are identical to those in present work.

The corresponding Ragone plot of the ASC and several other ZnO-based hybrid materials reported in the literature are presented in Fig. 7(d) [62–68]. The device reaches a high energy density of 30.6 $W \cdot h \cdot kg^{-1}$ at a power density of 398 $W \cdot kg^{-1}$, and even maintains 10.1 $W \cdot h \cdot kg^{-1}$ at a high-power density of 8,000 $W \cdot kg^{-1}$. The cycling performance of the Ni/ZnO-600//AC asymmetric supercapacitors is evaluated at a high current density of 5 $A \cdot g^{-1}$ (Fig. 7(e)). After 5,000 cycles, the device maintained 89% of its original performance.

4 Conclusions

We successfully designed and fabricated Ni/ZnO nanocomposites for high-performance supercapacitors. The Ni/ZnO-600 electrode shows specific capacitance of 807 $F \cdot g^{-1}$ at 1 $A \cdot g^{-1}$. The electrode also exhibits excellent cyclic stability, and 86%

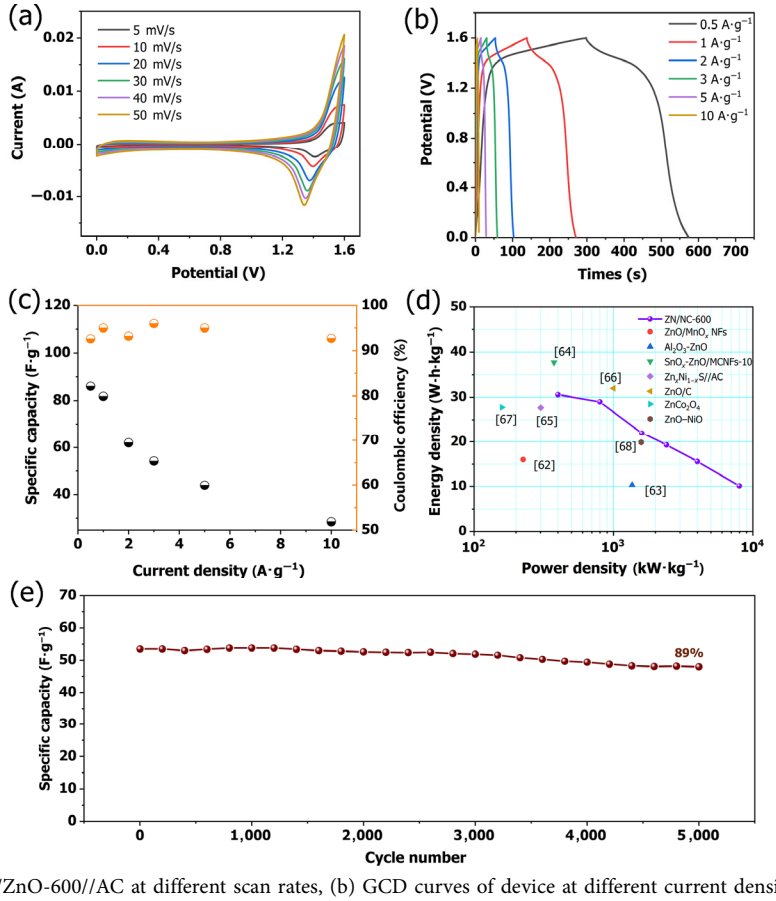

Figure 7 (a) CV curves of Ni/ZnO-600//AC at different scan rates, (b) GCD curves of device at different current densities, (c) specific capacitance at different current densities and Coulomb efficiency of the device at a current density in the range of 0.5–10 $A \cdot g^{-1}$, (d) Ragone plots of the device and other hybrid materials reported in the literature, and (e) cycling stability of the device tested after 5,000 cycles at 5 $A \cdot g^{-1}$.

capacitance retention after 5,000 cycles at 10 $A \cdot g^{-1}$. The energy densities of the asymmetric device are 30.6 and 10.1 $W \cdot h \cdot kg^{-1}$ at power densities of 400 and 8,000 $W \cdot kg^{-1}$, respectively.

Therefore, we suggest that the greatly improved electrochemical properties of the Ni/ZnO nano-sponges are attributed to the synergistic effects: (i) well-crystallized ZnO NPs and stable 3D porous carbon structure; (ii) synergistic effect between carbon materials and NiO/ZnO; (iii) high conductivity of carbon and metal Ni, which improves the charge transport; and (iv) annealing that induces oxygen and nickel deficiencies in ZnO and NiO to improve the charge transport and provide additional electrochemical active sites.

The ZnO-based nanocomposite with remarkable electrochemical properties is a potential material for high-performance energy storage systems. Other metal oxide-based nanocomposites with high surface defects can also be obtained by using a similar synthetic strategy.

Acknowledgements

This work was supported by the National Natural Science Foundation of China (Nos. 11975043 and 11605007).

Electronic Supplementary Material: Supplementary material (Lorentz curve fitting of Raman spectra, SEM images of Ni-MOF precursor, EDS of samples, TEM and HRTEM images of Ni/ZnO-400 and Ni/ZnO-500, the diagram of particle size distribution, nitrogen adsorption/desorption isotherms of samples, high resolution spectra of C1s, CV, and GCD curves of the Ni/ZnO-400, Ni/ZnO-500, ZnO, and NiO) is available in the online version of this article at https://doi.org/10.1007/s12274-021-3341-z.

References

[1] Liu, C.; Li, F.; Ma, L. P.; Cheng, H. M. Advanced materials for energy storage. *Adv. Mater.* **2010**, *22*, E28–E62.

[2] Wang, J. S.; Zhang, X.; Li, Z.; Ma, Y. Q.; Ma, L. Recent progress of biomass-derived carbon materials for supercapacitors. *J. Power Sources* **2020**, *451*, 227794.

[3] Hussain, N.; Wu, F. F.; Xu, L. Q.; Qian, Y. T. $Co_{0.85}Se$ hollow spheres constructed of ultrathin 2D mesoporous nanosheets as a novel bifunctional-electrode for supercapacitor and water splitting. *Nano Res.* **2019**, *12*, 2941–2946.

[4] Chen, T.; Li, M.; Song, S.; Kim, P.; Bae, J. Biotemplate preparation of multilayered TiC nanoflakes for high performance symmetric supercapacitor. *Nano Energy* **2020**, *71*, 104549.

[5] Li, W. H.; Ding, K.; Tian, H. R.; Yao, M. S.; Nath, B.; Deng, W. H.; Wang, Y. B.; Xu, G. Conductive metal-organic framework nanowire array electrodes for high-performance solid-state supercapacitors. *Adv. Funct. Mater.* **2017**, *27*, 1702067.

[6] Tong, L.; Jiang, C.; Cai, K. F.; Wei, P. High-performance and freestanding PPy/$Ti_3C_2T_x$ composite film for flexible all-solid-state supercapacitors. *J. Power Sources* **2020**, *465*, 228267.

[7] Li, M. P.; El-Kady, M. F.; Hwang, J. Y.; Kowal, M. D.; Marsh, K.; Wang, H. S.; Zhao, Z. J.; Kaner, R. B. Embedding hollow Co_3O_4 nanoboxes into a three-dimensional macroporous graphene framework for high-performance energy storage devices. *Nano Res.* **2018**, *11*, 2836–2846.

[8] Chen, Y. Z.; Zhou, T. F.; Li, L.; Pang, W. K.; He, X. M.; Liu, Y. N.; Guo, Z. P. Interfacial engineering of nickel boride/metaborate and its effect on high energy density asymmetric supercapacitors. *ACS Nano* **2019**, *13*, 9376–9385.

[9] Wang, Z.; Jia, W.; Jiang, M. L.; Chen, C.; Li, Y. D. One-step accurate synthesis of shell controllable $CoFe_2O_4$ hollow microspheres as high-performance electrode materials in supercapacitor. *Nano Res.* **2016**, *9*, 2026–2033.

[10] Selvakumar, M.; Bhat, D. K.; Aggarwal, A. M.; Iyer, S. P.; Sravani, G. Nano ZnO-activated carbon composite electrodes for supercapacitors. *Phys. B: Condens Matter* **2010**, *405*, 2286–2289.

[11] Ouyang, Y.; Xia, X. F.; Ye, H. T.; Wang, L.; Jiao, X. Y.; Lei, W.; Hao, Q. L. Three-dimensional hierarchical structure ZnO@C@NiO on carbon cloth for asymmetric supercapacitor with enhanced cycle stability. *ACS Appl. Mater. Interfaces* **2018**, *10*, 3549–3561.

[12] He, X. L.; Yoo, J. E.; Lee, M. H.; Bae, J. Morphology engineering of ZnO nanostructures for high performance supercapacitors: Enhanced electrochemistry of ZnO nanocones compared to ZnO nanowires. *Nanotechnology* **2017**, *28*, 245402.

[13] Wang, X. S.; Pan, Z. H.; Wu, Y.; Ding, X. Y.; Hong, X. J.; Xu, G. G.; Liu, M. N.; Zhang, Y. G.; Li, W. S. Infiltrating lithium into carbon cloth decorated with zinc oxide arrays for dendrite-free lithium metal anode. *Nano Res.* **2018**, *12*, 525–529.

[14] Fang, L. X.; Zhang, B. L.; Li, W.; Zhang, J. Z.; Huang, K. J.; Zhang, Q. Y. Fabrication of highly dispersed ZnO nanoparticles embedded in graphene nanosheets for high performance supercapacitors. *Electrochim. Acta* **2014**, *148*, 164–169.

[15] Lu, Z. Y.; Chang, Z.; Liu, J. F.; Sun, X. M. Stable ultrahigh specific capacitance of NiO nanorod arrays. *Nano Res.* **2011**, *4*, 658.

[16] Lu, Z. Y.; Chang, Z.; Zhu, W.; Sun, X. M. Beta-phased $Ni(OH)_2$ nanowall film with reversible capacitance higher than theoretical Faradic capacitance. *Chem. Commun.* **2011**, *47*, 9651–9653.

[17] Meng, G.; Yang, Q.; Wu, X. C.; Wan, P. B.; Li, Y. P.; Lei, X. D.; Sun, X. M.; Liu, J. F. Hierarchical mesoporous NiO nanoarrays with ultrahigh capacitance for aqueous hybrid supercapacitor. *Nano Energy* **2016**, *30*, 831–839.

[18] Zhi, M. J.; Xiang, C. C.; Li, J. T.; Li, M.; Wu, N. Q. Nanostructured carbon-metal oxide composite electrodes for supercapacitors: A review. *Nanoscale* **2013**, *5*, 72–88.

[19] Gao, P.; Chen, Z.; Gong, Y. X.; Zhang, R.; Liu, H.; Tang, P.; Chen, X. H.; Passerini, S.; Liu, J. L. The role of cation vacancies in electrode materials for enhanced electrochemical energy storage: Synthesis, advanced characterization, and fundamentals. *Adv. Energy Mater.* **2020**, *10*, 1903780.

[20] Wang, J.; Chen, R. S.; Xiang, L.; Komarneni, S. Synthesis, properties and applications of ZnO nanomaterials with oxygen vacancies: A review. *Ceram. Int.* **2018**, *44*, 7357–7377.

[21] Bi, W. C.; Wu, Y. J.; Liu, C. F.; Wang, J. C.; Du, Y. C.; Gao, G. H.; Wu, G. M.; Cao, G. Z. Gradient oxygen vacancies in V_2O_5/PEDOT nanocables for high-performance supercapacitors. *ACS Appl. Energy Mater.* **2019**, *2*, 668–677.

[22] Du, Y. H.; Wang, X. Y.; Sun, J. C. Tunable oxygen vacancy concentration in vanadium oxide as mass-produced cathode for aqueous zinc-ion batteries. *Nano Res.* **2020**, *14*, 754–761.

[23] Cai, Z.; Bi, Y. M.; Hu, E. Y.; Liu, W.; Dwarica, N.; Tian, Y.; Li, X. L.; Kuang, Y.; Li, Y. P.; Yang, X. Q. et al. Single-crystalline ultrathin Co_3O_4 nanosheets with massive vacancy defects for enhanced electrocatalysis. *Adv. Energy Mater.* **2018**, *8*, 1701694.

[24] Salunkhe, R. R.; Kaneti, Y. V.; Yamauchi, Y. Metal-organic framework-derived nanoporous metal oxides toward supercapacitor applications: Progress and prospects. *ACS Nano* **2017**, *11*, 5293–5308.

[25] Cruz-Navarro, J. A.; Hernandez-Garcia, F.; Romero, G. A. A. Novel applications of metal-organic frameworks (MOFs) as redox-active materials for elaboration of carbon-based electrodes with electroanalytical uses. *Coord. Chem. Rev.* **2020**, *412*, 213263.

[26] Liu, S. T.; Zhou, J. S.; Song, H. H. 2D Zn-hexamine coordination frameworks and their derived N-rich porous carbon nanosheets for ultrafast sodium storage. *Adv. Energy Mater.* **2018**, *8*, 1800569.

[27] Hendon, C. H.; Rieth, A. J.; Korzyński, M. D.; Dincă, M. Grand challenges and future opportunities for metal-organic frameworks. *ACS Cent. Sci.* **2017**, *3*, 554–563.

[28] Jiao, Y.; Hong, W. Z.; Li, P. Y.; Wang, L. X.; Chen, G. Metal-organic framework derived Ni/NiO micro-particles with subtle lattice distortions for high-performance electrocatalyst and supercapacitor. *Appl. Catal. B Environ.* **2019**, *244*, 732–739.

[29] Dillip, G. R.; Banerjee, A. N.; Anitha, V. C.; Raju, B. D. P.; Joo, S. W.; Min, B. K. Oxygen vacancy-induced structural, optical, and enhanced supercapacitive performance of zinc oxide anchored graphitic carbon nanofiber hybrid electrodes. *ACS Appl. Mater. Interfaces* **2016**, *8*, 5025–5039.

[30] Katea, S. N.; Hajduk, Š.; Orel, Z. C.; Westin, G. Low cost, fast solution synthesis of 3D framework ZnO nanosponges. *Inorg. Chem.*

2017, *56*, 15150–15158.
[31] Anžlovar, A.; Kogej, K.; Orel, Z. C.; Žigon, M. Impact of inorganic hydroxides on ZnO nanoparticle formation and morphology. *Cryst. Growth Des*. **2014**, *14*, 4262–4269.
[32] Shingange, K.; Swart, H. C.; Mhlongo, G. H. H_2S detection capabilities with fibrous-like La-doped ZnO nanostructures: A comparative study on the combined effects of La-doping and post-annealing. *J. Alloys Compd*. **2019**, *797*, 284–301.
[33] Chan, Y. C.; Yu, J.; Ho, D. Morphology, stoichiometry, and crystal structure control via post-annealing for Pt–ZnO nanograin Schottky barrier interfaces. *Appl. Surf. Sci*. **2018**, *443*, 506–514.
[34] Namoune, A.; Touam, T.; Chelouche, A. Thickness, annealing and substrate effects on structural, morphological, optical and waveguiding properties of RF sputtered ZnO thin films. *J. Mater. Sci.: Mater. Electron*. **2017**, *28*, 12207–12219.
[35] Naeem, F.; Naeem, S.; Zhao, Z.; Shu, G. Q.; Zhang, J.; Mei, Y. F.; Huang, G. S. Atomic layer deposition synthesized ZnO nanomembranes: A facile route towards stable supercapacitor electrode for high capacitance. *J. Power Sources* **2020**, *451*, 227740.
[36] Guerra, A.; Achour, A.; Vizireanu, S.; Dinescu, G.; Messaci, S.; Hadjersi, T.; Boukherroub, R.; Coffinier, Y.; Pireaux, J. J. ZnO/Carbon nanowalls shell/core nanostructures as electrodes for supercapacitors. *Appl. Surf. Sci*. **2019**, *481*, 926–932.
[37] Reddy, I. N.; Reddy, C. V.; Sreedhar, A.; Shim, J.; Cho, M.; Yoo, K.; Kim, D. Structural, optical, and bifunctional applications: Supercapacitor and photoelectrochemical water splitting of Ni-doped ZnO nanostructures. *J. Electroanal. Chem*. **2018**, *828*, 124–136.
[38] Jaramillo, A. F.; Baez-Cruz, R.; Montoya, L. F.; Medinam, C.; Pérez-Tijerina, E.; Salazar, F.; Rojas, D.; Melendrez, M. F. Estimation of the surface interaction mechanism of ZnO nanoparticles modified with organosilane groups by Raman Spectroscopy. *Ceram. Int*. **2017**, *43*, 11838–11847.
[39] Chen, S. J.; Liu, Y. C.; Shao, C. L.; Mu, R.; Lu, Y. M.; Zhang, J. Y.; Shen, D. Z.; Fan, X. W. Structural and optical properties of uniform ZnO nanosheets. *Adv. Mater*. **2005**, *17*, 586–590.
[40] Serrano, J.; Romero, A. H.; Manjón, F. J.; Lauck, R.; Cardona, M.; Rubio, A. Pressure dependence of the lattice dynamics of ZnO: An *ab initio* approach. *Phys. Rev. B* **2004**, *69*, 094306.
[41] Xu, J.; Li, M.; Yang, L. Y.; Qiu, J. H.; Chen, Q.; Zhang, X. F.; Feng, Y.; Yao, J. F. Synergy of Ni dopant and oxygen vacancies in ZnO for efficient photocatalytic depolymerization of sodium lignosulfonate. *Chem. Eng. J*. **2020**, *394*, 125050.
[42] Wang, Y. Y.; Xiao, X.; Li, Q.; Pang, H. Synthesis and progress of new oxygen-vacant electrode materials for high-energy rechargeable battery applications. *Small* **2018**, *14*, 1802193.
[43] Zhou, D. J.; Xiong, X. Y.; Cai, Z.; Han, N. N.; Jia, Y.; Xie, Q. X.; Duan, X. X.; Xie, T. H.; Zheng, X. L.; Sun, X. M. et al. Flame-engraved nickel-iron layered double hydroxide nanosheets for boosting oxygen evolution reactivity. *Small Methods* **2018**, *2*, 1800083.
[44] Zannotti, M.; Benazzi, E.; Stevens, L. A.; Minicucci, M.; Bruce, L.; Snape, C. E.; Gibson, E. A.; Giovannetti, R. Reduced graphene oxide-NiO photocathodes for p-type dye-sensitized solar cells. *ACS Appl. Energy Mater*. **2019**, *2*, 7345–7353.
[45] Duan, W. J.; Lu, S. H.; Wu, Z. L.; Wang, Y. S. Size effects on properties of NiO nanoparticles grown in alkalisalts. *J. Phys. Chem. C* **2012**, *116*, 26043–26051.
[46] Sunny, A.; Balasubramanian, K. Raman spectral probe on size-dependent surface optical phonon modes and magnon properties of NiO nanoparticles. *J. Phys. Chem. C* **2020**, *124*, 12636–12644.
[47] Kaschner, A.; Haboeck, U.; Strassburg, M.; Strassburg, M.; Kaczmarczyk, G.; Hoffmann, A.; Thomsen, C.; Zeuner, A.; Alves, H. R.; Hofmann, D. M. et al. Nitrogen-related local vibrational modes in ZnO: N. *Appl. Phys. Lett*. **2002**, *80*, 1909–1911.
[48] Dong, J. J.; Zhang, X. W.; You, J. B.; Cai, P. F.; Yin, Z. G.; An, Q.; Ma, X. B.; Jin, P.; Wang, Z. G.; Chu, P. K. Effects of hydrogen plasma treatment on the electrical and optical properties of ZnO films: Identification of hydrogen donors in ZnO. *ACS Appl. Mater. Interfaces* **2010**, *2*, 1780–1784.
[49] Rana, A. K.; Kumar, Y.; Rajput, P.; Jha, S. N.; Bhattacharyya, D.; Shirage, P. M. Search for origin of room temperature ferromagnetism properties in Ni-doped ZnO nanostructure. *ACS Appl. Mater. Interfaces* **2017**, *9*, 7691–7700.
[50] Manjón, F. J.; Marí, B.; Serrano, J.; Romero, A. H. Silent Raman modes in zinc oxide and related nitrides. *J. Appl. Phys*. **2005**, *97*, 053516.
[51] He, J. J.; Zhang, D. Y.; Wang, Y. L.; Zhang, J. W.; Yang, B. B.; Shi, H.; Wang, K. J.; Wang, Y. Biomass-derived porous carbons with tailored graphitization degree and pore size distribution for supercapacitors with ultra-high rate capability. *Appl. Surf. Sci*. **2020**, *515*, 146020.
[52] Fu, F. B.; Yang, D. J.; Wang, H.; Qian, Y.; Yuan, F.; Zhong, J. Q.; Qiu, X. Q. Three-dimensional porous framework lignin-derived carbon/ZnO composite fabricated by a facile electrostatic self-assembly showing good stability for high-performance supercapacitors. *ACS Sustainable Chem. Eng*. **2019**, *7*, 16419–16427.
[53] Obradovic, N.; Stevanovic, S.; Zeljkovic, V.; Ristic, M. M. Influence of ZnO specific surface area on its sintering kinetics. *Powder Metall. Met. Ceram*. **2009**, *48*, 182–185.
[54] Park, K.; Zhang, Q. F.; Garcia, B. B.; Cao, G. Z. Effect of annealing temperature on TiO_2–ZnO core–shell aggregate photoelectrodes of dye-sensitized solar cells. *J. Phys. Chem. C* **2011**, *115*, 4927–4934.
[55] Zhao, Y. F.; Jia, X. D.; Chen, G. B.; Shang, L.; Waterhouse, G. I. N.; Wu, L. Z.; Tung, C. H.; O'Hare, D.; Zhang, T. R. Ultrafine NiO nanosheets stabilized by TiO_2 from monolayer NiTi-LDH precursors: An active water oxidation electrocatalyst. *J. Am. Chem. Soc*. **2016**, *138*, 6517–6524.
[56] Wang, J. S.; Jin, H. H.; Wang, W. H.; Zhao, Y. H.; Li, Y.; Bao, M. Ultrasmall Ni-ZnO/SiO_2 synergistic catalyst for highly efficient hydrogenation of $NaHCO_3$ to formic acid. *ACS Appl. Mater. Interfaces* **2020**, *12*, 19581–19586.
[57] Arunpandiyan, S.; Bharathi, S.; Pandikumar, A.; Arasi, S. E.; Arivarasan, A. Structural analysis and redox additive electrolyte based supercapacitor performance of ZnO/CeO_2 nanocomposite. *Mater. Sci. Semicond. Process*. **2020**, *106*, 104765.
[58] Li, Y.; Wei, Q. L.; Wang, R.; Zhao, J. K.; Quan, Z. L.; Zhan, T. R.; Li, D. X.; Xu, J.; Teng, H. N.; Hou, W. G. 3D hierarchical porous nitrogen-doped carbon/Ni@NiO nanocomposites self-templated by cross-linked polyacrylamide gel for high performance supercapacitor electrode. *J. Colloid Interface Sci*. **2020**, *570*, 286–299.
[59] Mahajan, H.; Bae, J.; Yun, K. Facile synthesis of ZnO-Au nanocomposites for high-performance supercapacitors. *J. Alloys Compd*. **2018**, *758*, 131–139.
[60] Yang, P.; Song, X. L.; Jia, C. C.; Chen, H. S. Metal-organic framework-derived hierarchical ZnO/NiO composites: Morphology, microstructure and electrochemical performance. *J. Ind. Eng. Chem*. **2018**, *62*, 250–257.
[61] Wu, G. Y.; Song, Y.; Wan, J. F.; Zhang, C. W.; Yin, F. X. Synthesis of ultrafine ZnO nanoparticles supported on nitrogen-doped ordered hierarchically porous carbon for supercapacitor. *J. Alloys Compd*. **2019**, *806*, 464–470.
[62] Samuel, E.; Joshi, B.; Kim, Y. I.; Aldalbahi, A.; Rahaman, M.; Yoon, S. S. ZnO/MnO_x nanoflowers for high-performance supercapacitor electrodes. *ACS Sustainable Chem. Eng*. **2020**, *8*, 3697–3708.
[63] Di, S.; Gong, L. G.; Zhou, B. B. Precipitated synthesis of Al_2O_3-ZnO nanorod for high-performance symmetrical supercapacitors. *Mater. Chem. Phys*. **2020**, *253*, 123289.
[64] Liu, J.; Xu, T.; Sun, X. W.; Bai, J.; Li, C. P. Preparation of stable composite porous nanofibers carried SnO_x-ZnO as a flexible supercapacitor material with excellent electrochemical and cycling performance. *J. Alloys Compd*. **2019**, *807*, 151652.
[65] Mao, X. Q.; Wang, W. Z.; Wang, Z. H. Hydrothermal synthesis of $Zn_xNi_{1-x}S$ nanosheets for hybrid supercapacitor applications. *ChemPlusChem* **2017**, *82*, 1145–1152.
[66] Sasirekha, C.; Arumugam, S.; Muralidharan, G. Green synthesis of ZnO/carbon (ZnO/C) as an electrode material for symmetric supercapacitor devices. *Appl. Surf. Sci*. **2018**, *449*, 521–527.
[67] Shang, Y. Y.; Xie, T.; Ma, C. L.; Su, L. H.; Gai, Y. S.; Liu, J.; Gong, L. Y. Synthesis of hollow $ZnCo_2O_4$ microspheres with enhanced electrochemical performance for asymmetric supercapacitor. *Electrochim. Acta* **2018**, *286*, 103–113.
[68] Pang, H.; Ma, Y. H.; Li, G. C.; Chen, J.; Zhang, J. S.; Zheng, H. H.; Du, W. M. Facile synthesis of porous ZnO-NiO composite micropolyhedrons and their application for high power supercapacitor electrode materials. *Dalton Trans*. **2012**, *41*, 13284–13291.